Monthly Notices of the ROYAL ASTRONOMICAL SOCIETY

MNRAS **527,** 11507–11520 (2024) https://doi.org/10.1093/mnras/stad3989
Advance Access publication 2023 December 27

GRB 201015A: from seconds to months of optical monitoring and supernova discovery

S. Belkin [1,2,3★] A. S. Pozanenko,[1,2,4] P. Y. Minaev [2,5] N. S. Pankov,[1,2] A. A. Volnova,[2] A. Rossi [6] G. Stratta [6,7,8] S. Benetti [9] E. Palazzi,[6] A. S. Moskvitin,[10] O. Burhonov,[11] V. V. Rumyantsev,[12] E. V. Klunko,[13] R. Ya. Inasaridze,[14] I. V. Reva,[15] V. Kim [15,16] M. Jelinek,[17] D. A. Kann,[18] A. E. Volvach,[12] L. N. Volvach,[12] D. Xu,[19] Z. Zhu,[19] S. Fu[19] and A. A. Mkrtchyan[4]

Affiliations are listed at the end of the paper

Accepted 2023 December 21. Received 2023 December 1; in original form 2023 September 18

ABSTRACT

We present full photometric coverage and spectroscopic data for soft gamma-ray burst GRB 201015A with a redshift $z = 0.426$. Our data span a time range of 85 d following the detection of GRB. These observations revealed an underlying supernova SN 201015A with a maximum at 8.54 ± 1.48 d (rest frame) and an optical peak absolute magnitude $-19.45^{+0.85}_{-0.47}$ mag. The SN stands out clearly, since the contribution of the afterglow at this time is not dominant, which made it possible to determine SN's parameters. A comparison of these parameters reveals that the SN 201015A is the earliest (the minimum $T_{\rm max}$) known SN associated with GRBs. Spectroscopic observations during the SN decay stage showed broad lines, indicating a large photospheric velocity, and identified this SN as a Type Ic-BL. Thus, the SN 201015A associated with the GRB 201015A becomes the 27th SN/GRB confirmed by both photometric and spectroscopic observations. Using the results of spectral analysis based on the available data of *Fermi*-GBM experiment, the parameters $E_{\rm p,i} = 20.0 \pm 8.5$ keV and $E_{\rm iso} = (1.1 \pm 0.2) \times 10^{50}$ erg were obtained. According to the position of the burst on the $E_{\rm p,i}$–$E_{\rm iso}$ correlation, GRB 201015A was classified as a type II (long) GRB, which was also confirmed by the $T_{90,\rm i}$–*EH* diagram.

Key words: gamma-ray bursts – transients: supernovae.

1 INTRODUCTION

In recent years, extensive optical observations of gamma-ray bursts (GRBs) have revealed a physical relationship between long-duration ($T_{90} \gtrsim 2$ s; see Kouveliotou et al. 1993; Koshut et al. 1996) GRBs and core-collapse supernovae (SNe; e.g. Cano et al. 2017b). The first reliable evidence of such an association was found between GRB 980425 and SN 1998bw. Type broad-lined supernova (Ic-BL SN) 1998bw was determined to be temporally and spatially consistent with GRB 980425 (Galama et al. 1998; Iwamoto et al. 1998; Kulkarni et al. 1998). Then, the very bright event GRB 030329 was confirmed to be associated with SN 2003dh (Hjorth et al. 2003; Matheson et al. 2003; Stanek et al. 2003), which was also classified as Type Ic-BL. As of today, there is no unequivocal distinction between SN Ic and SN Ic-BL. It is considered that SNe Ic-BL are SNe Ic with a higher photospheric velocity approaching 15 000–30 000 km s^{-1} and absence of the H and He in the spectra (e.g. Modjaz et al. 2016). In comparison with ordinary SNe, the kinetic energy of these two mentioned events exceeded 10^{52} erg. Such highly energetic SNe were named hypernovae (e.g. Paczyński 1998).

As a result of numerous observations, it is possible to indicatively divide the optical light curve of long GRB into four successively alternating phases (e.g. Pozanenko et al. 2021). The prompt emission phase can barely be observed due to the relatively slow response of the ground-based observatories to the GRB detection alerts.

The prompt emission phase is followed by the afterglow stage. It is usually the longest one and can be described by a power law or a power law with a jet break (see e.g. Sari, Piran & Halpern 1999). At this stage, inhomogeneities, characterized by a statistically significant deviation of data points from the power-law decay of the afterglow, can occur (e.g. Mazaeva, Pozanenko & Minaev 2018). The light curve of the early GRB 201015A afterglow indicates the presence of a bump with a peak at ∼6.6 min post trigger that deviates substantially from the power-law slope of the afterglow. There are a number of models to describe this behaviour, see Ror et al. (2023) for details.

Further, the bumps identified in the light curves of GRB about 7–30 d after the burst were interpreted as an SN explosion with an expansion of its photosphere, followed by an increase in luminosity (e.g. Bloom et al. 1999; Garnavich et al. 2003). The radiation of an SN manifests itself when the central engine's activity has long ceased, and there is nowhere to take an additional powerful source of energy. Spectroscopic observations showed that spectra measured during the SN phase are usually characterized by broad lines and the absence of hydrogen and helium lines, which is one of the hallmarks of Type Ic-BL SNe. See Section 3.3 for details related to the SN associated with the GRB 201015A.

Finally, the source fades, causing the afterglow flux of the GRB, and the SN radiation to drop below the luminosity level

★ E-mail: sergey.belkin@monash.edu

Table 1. The main parameters of GRB 201015A.

Parameter	Value	Reference
RA(J2000)	23 h 37 m 16.41 s	Malesani, de Ugarte Postigo & Pursimo (2020)
Dec.(J2000)	+53 d 24′ 56.5″	Malesani, de Ugarte Postigo & Pursimo (2020)
z	0.426	de Ugarte Postigo et al. (2020)
$D^{a}{}_{L}$	2363.6 Mpc	Wright (2006)
$A_{\rm R}$	0.375	Schlafly & Finkbeiner (2011)
$T_{90,\rm i}$ (*Fermi*-GBM)	11.5 ± 2.5 s	Online *Fermi* catalogue
$E_{\rm iso}$	(1.1 ± 0.2) × 10^{50} erg	Online *Fermi* catalogue; this work
$E_{\rm p,i}$	20.0 ± 8.5 keV	Online *Fermi* catalogue; this work
Offset	1.5″ (8.453 kpc)	This work

[a]Calculated using $H_0 = 69.6$ km s^{-1} Mpc^{-1}, $\Omega_{\rm M} = 0.286$, $\Omega_\Lambda = 0.714$ (Bennett et al. 2014).

of the host galaxy. This is the final phase of the optical light curve. The study of this stage makes it possible to estimate both the integrated extinction within the host galaxy and its physical parameters.

This work is dedicated to a comprehensive study and description of the GRB 201015A and associated SN discovered both in photometric and spectroscopic data. Section 2 contains the description of the observations that led to the reported data. Information about the detection of prompt gamma-ray emission and its classification is presented in Section 3.1. Section 3.2 is dedicated to the both early- and late-time afterglow and its analysis. A discussion of the results of afterglow observations in the X-ray range is also given. The description and analysis of photometric and spectroscopic observations of an SN associated with a GRB 201015A are given in Section 3.3. Information about the host galaxy of the GRB 201015A is presented in Section 3.4. All results of observations, processing, and interpretation are discussed in Section 3 and summarized in Section 4.

2 OBSERVATIONS

At 22:50:13 UT (=T_0 hereafter) on 2020 October 15 (D'Elia et al. 2020), GRB 201015A was initially detected by the Burst Alert Telescope (BAT; Barthelmy et al. 2005) aboard the *Neil Gehrels Swift Observatory* (henceforth *Swift*) with duration of $T_{90} \approx 10$ s and relatively soft energy spectrum (Markwardt et al. 2020). *Swift* was not able to slew immediately to the burst due to an observing constraint. Later, the burst was also found in data of *Fermi*-GBM in a ground-based search of sub-threshold events (Fletcher, Veres & Fermi-GBM Team 2020).

2.1 X-ray imaging

The X-ray afterglow was detected and observed by the *Swift*'s X-ray telescope (XRT; Burrows et al. 2005). XRT began to observe the field of GRB 201015A only 3214.1 s after the BAT trigger (Kennea et al. 2020). Using XRT data and four Ultraviolet/Optical Telescope (Roming et al. 2005) images, an astrometrically corrected X-ray position was determined as following RA(J2000) = 23:37:16.96, Dec.(J2000) = +53:24:52.6 with an uncertainty of 3.8 arcsec (90 per cent confidence radius) (Kennea et al. 2020).

Consequently, 7200 s of XRT data for GRB 201015A from 3200 to 57 300 s after the BAT trigger were obtained. The light curve in this time interval is preliminarily described with a single power law with a decay index $\alpha = 1.49^{+0.24}_{-0.21}$ (D'Ai et al. 2020).

2.2 Optical observations

Optical observations of the field of GRB 201015A were carried out with the ZTSh telescope (Rumyantsev, Kiselev & Ivanova 2019) of Crimean Astrophysical Observatory (CrAO; Severny 1955), the AZT-33IK telescope of the Sayan Observatory (Mondy, Chuprakov, Eselevich & Korobtsev 2018), the AS-32 telescope of Abastumani Astrophysical Observatory (AbAO; Khetsuriani 1967), the Zeiss-1000 telescope of Special Astrophysical Observatory of the Russian Academy of Sciences (SAO RAS; Shvedova 1995), the Zeiss-1000 telescope of Tien Shan Astronomical Observatory (TSHAO; Elenin, Kusakin & Molotov 2015), the AZT-22 telescope of Maidanak Observatory (MAO; Ehgamberdiev et al. 2000), the AZT-20 telescope of Assy-Turgen Observatory (ATO; Serebryanskiy et al. 2018), the LBT telescope (Hill & Salinari 1994) of Mount Graham International Observatory (MGIO; Sage 2003), the FRAM (Prouza et al. 2010), and GTC (Rodríguez-Espinosa & Alvarez Martin 1997) telescopes of Roque de los Muchachos Observatory (ORM; Ardeberg 1984), the NEXT telescope of Xinjiang Astronomy Observatory (XAO) and the 2.16-m telescope (Zhou et al. 2016) of the Xinglong Observatory (XO) in a sufficient number of imaging epochs. The characteristics of the telescopes used are presented in Table 2.

The earliest observations were made using the 25-cm FRAM-ORM robotic telescope at La Palma (Spain) which automatically responded to the alert regarding GRB 201015A (D'Elia et al. 2020) and obtained a series of unfiltered images with an exposure of 20 s, starting at 22:50:50.8 UT, i.e. 37.6 s since trigger (see Jelinek et al. 2020; Ror et al. 2023).

Observations with the 2.6-m ZTSh telescope of CrAO observatory between October 16 (UT) 01:02:14 and 02:52:23 (∼2.3 to ∼4 h post-burst trigger) were carried out in *White* and *R* filters. The optical counterpart was clearly detected in each frame of 120 s exposure in the *R* filter (Belkin et al. 2020b). The magnitude at this epoch was *R* ∼ 20.7 mag and showed a power-law decay.

Subsequent observations of the optical afterglow were conducted using the 1.6-m AZT-33IK telescope of Mondy observatory, the 0.7-m AS-32 telescope of Abastumani Observatory, the 1.5-m AZT-20 telescope of ATO, and the 1-m Zeiss-1000 telescope of SAO RAS of the GRB-IKI follow-up network (FuN). Altogether these observations spanned the time range from 2.3 h to 85 d after the GRB 201015A detection.

Spectroscopic observations of the GRB 201015A were carried out with the Multi-Object Double Spectrographs MODS-1 and MODS-2 instruments (Pogge et al. 2010) mounted on the 2 × 8.4-m LBT telescope (Mt Graham, AZ, USA) at the mid-time of 04:00 UT on 2020 November 13, ∼28.8 d after the burst trigger (Rossi et al. 2021).

Observations were also conducted on the facilities of other groups (Ackley et al. 2020; Grossan et al. 2020; Hu et al. 2020; Jelinek

Table 2. The telescopes used to observe the burst in the optical band.

Observatory	Location	Telescope	Diameter[a]	Field of view
CrAO	Nauchny/Crimea	ZTSh	2.6	14′.4 × 14′.4
Mondy	Sayan	AZT-33IK	1.6	6′.7 × 7′.9
AbAO	Abastumani, Georgia	AS-32	0.7	44′.4 × 44′.4
SAO RAS	Arhyz	Zeiss-1000 (S)	1.0	7′.05 × 7′.36
TSHAO	Tien-Shan	Zeiss-1000 (T)	1.0	19′.2 × 19′.2
MAO	Maidanak	AZT-22	1.5	18′.3 × 18′.3
ATO	Assy-Turgen	AZT-20	1.5	22′.3 × 22′.3
MGIO	Arizona	LBT	8.6	6′.0 × 6′.0
ORM	The Canary Islands	GTC	10.4	8′.0 × 9′.7
XAO	Xinjiang	NEXT	0.6	21′.6 × 21′.8
XO	Xinglong	Xinglong-2.16m	2.16	9′.4 × 9′.4

[a]The diameter (size) of the primary mirror, m.

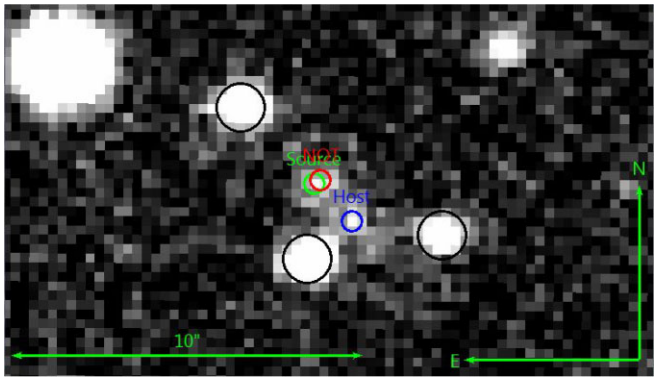

Figure 1. The finding chart image of GRB 201015A. The source is denoted by a small left circle. The localisation of the source determined from the results of observations with the Nordic Optical Telescope (NOT; Malesani, de Ugarte Postigo & Pursimo 2020), is represented by an upper small circle. A separate small circle marks the position of the proposed host galaxy. The bigger circles indicate nearby sources.

et al. 2020; Kumar et al. 2020a, b; Lipunov et al. 2020; Malesani, de Ugarte Postigo & Pursimo 2020; Rastinejad et al. 2020; Zhu et al. 2020a,b).

Analysis of the acquired images reveals the presence of several objects in the immediate vicinity of the source (Fig. 1). As a result, the most significant contribution to the resulting light curve was made by observations with telescopes featuring the smallest pixel scales (e.g. AZT-22, GTC, LBT). None the less, this does not diminish the contribution of observations at other observatories.

2.3 Radio observations

The observations at 36.8 GHz were carried out with the 22-m RT-22 radio telescope at the foot of Mount Koshka (Simeiz, Crimea). The antenna beam width at half-maximum is 100 arcsec. The radio telescope was pointed towards the source alternately by one and the other beam lobes forming under diagram modulation and having mutually orthogonal polarisations.

The antenna temperature from the source was determined as the difference between the radiometer responses averaged over 30 s at two different antenna positions. A series of 200–250 measurements were carried out, whereupon the average signal was calculated and its root-mean-square error was estimated. The measured antenna temperatures corrected for the absorption of emission in the Earth's atmosphere were converted to flux densities by comparing them with the results of observations of calibration sources (Volvach, Volvach & Larionov 2023). The results obtained from the observational data are presented in Table A1 and shown in Fig. 5.

2.4 Redshift determination

Spectroscopic observations of the afterglow of GRB 201015A were carried out with the 10.4-m GTC Telescope, at Roque de los Muchachos Observatory (La Palma, Spain) equipped with Optical System for Imaging and low-Intermediate-Resolution Integrated Spectroscopy (OSIRIS). It was conducted on 2020 October 16.172 UT (∼5.28 h after the GRB detection) and consisted of 3 s × 900 s exposures with the R1000B grism, covering the wavelength range from 370 to 780 nm. The spectrum showed a featureless continuum throughout the full spectral range. However, it was possible to identify emission features superposed on the trace, which were identified as [O III], [O II], and H β at a common redshift of 0.426 (de Ugarte Postigo et al. 2020).

The obtained redshift value was confirmed as a result of spectroscopic observations with the NOT, equipped with the Andalucia Faint Object Spectrograph and Camera (ALFOSC) spectrograph. The observations started on 2020 October 15.978 UT (38 min after the GRB detection) and consisted of 4 s × 900 s exposures with grism, covering the wavelength range from 380 to 940 nm.

Despite the trace visible across the full spectral range, weak absorption features were detected in a blue part of it and can be interpreted as Mg II, Mg I, and Ca II at the redshift of 0.423 (Izzo et al. 2020). Considering faint emission lines such as [O II] and H α also allows to confirm determined redshift. It sets a firm lower limit to the GRB's redshift, excluding a chance of superposition with a background galaxy.

3 DATA ANALYSIS AND RESULTS

3.1 Prompt emission (gamma-rays)

We use publicly available photon-by-photon (TTE) data of *Fermi*-GBM experiment[1] to analyse temporal properties of GRB 201015A. Background-subtracted light curve of GRB 201015A, constructed using data of most illuminated NaI_10 and NaI_11 detectors in the energy range of (6, 50) keV, is presented in Fig. 2. The burst is not visible in the energy range above 50 keV due to its soft spectrum. The light curve consists of the main emission episode with a duration

[1]ftp://legacy.gsfc.nasa.gov/fermi/data/

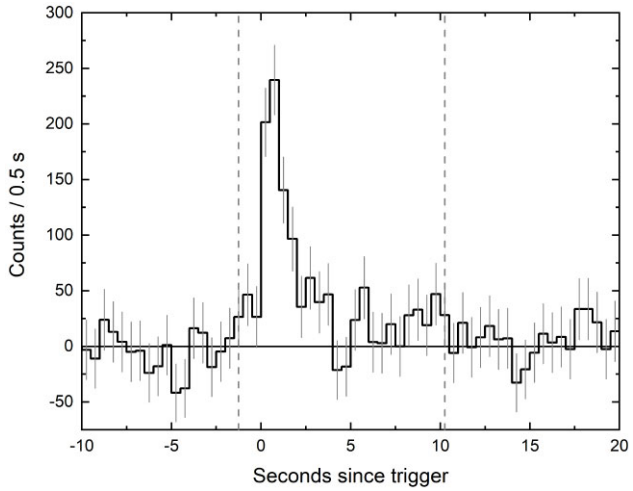

Figure 2. Background subtracted light curve of GRB 201015A in the energy range of (6, 50) keV with a time resolution of 0.5 s, based on *Fermi*-GBM data. Vertical dashed lines indicate T_{90} time interval ($T_{90} = 11.5 \pm 2.5$ s).

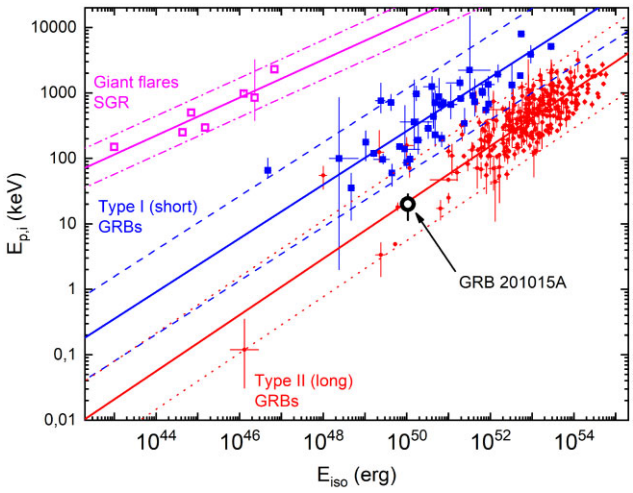

Figure 3. The $E_{\rm p,i}$–$E_{\rm iso}$ correlation for type I (blue squares), type II (red circles) GRBs, and soft gamma repeater (SGR) giant flares (magenta unfilled squares) with the approximation results, including $2\sigma_{\rm cor}$ correlation regions. The position of GRB 201015A (unfilled black circle) is typical for type II GRBs.

of about 2 s, followed by a weak tail with a total duration of $T_{90} = 11.5 \pm 2.5$ s (Fig. 2). The behaviour of the light curve is typical for type II (long) bursts, but the classification as type I (short) burst with extended emission is also possible (e.g. Norris & Bonnell 2006; Minaev, Pozanenko & Loznikov 2010a, b; Mozgunov, Minaev & Pozanenko 2021).

To classify GRB 201015A, we can use the method proposed in Minaev & Pozanenko (2020b), based on $E_{\rm p,i}$–$E_{\rm iso}$ correlation (e.g. Amati et al. 2002), as we know redshift of the source: $z = 0.426$ (de Ugarte Postigo et al. 2020). Using results of GRB 201015A spectral analysis, published in Fletcher, Veres & Fermi-GBM Team (2020), we obtain $E_{\rm p,i} = 20.0 \pm 8.5$ keV and $E_{\rm iso} = (1.1 \pm 0.2) \times 10^{50}$ erg. The position of GRB 201015A on $E_{\rm p,i}$–$E_{\rm iso}$ diagram is shown at Fig. 3, along with samples and correlation analysis results from Minaev & Pozanenko (2020a, b, 2021). The burst is placed close to the $E_{\rm p,i}$–$E_{\rm iso}$ correlation fit for type II (long) bursts,

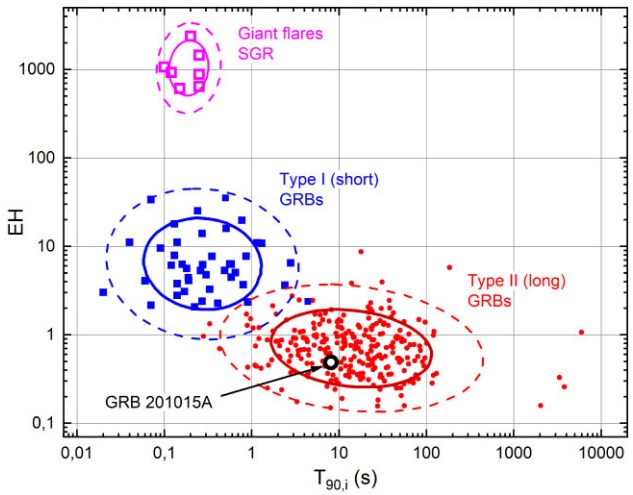

Figure 4. The $T_{90,\rm i}$–EH diagram for type I (blue squares), type II (red circles) GRBs, and SGR giant flares (magenta unfilled squares) with corresponding cluster analysis results (68 per cent and 95 per cent confidence regions are shown by bold solid and thin dashed curves, respectively). GRB 201015A (black unfilled circle) is within the 68 per cent confidence region of type II GRBs.

characterizing GRB 201015A as type II GRB (Minaev & Pozanenko 2020c).

The position of the burst at $E_{\rm p,i}$–$E_{\rm iso}$ correlation could be characterized by parameter $EH = \frac{(E_{\rm p,i}/100\ {\rm keV})}{(E_{\rm iso}/10^{51}\ {\rm erg})^{\ 0.4}}$, firstly introduced in Minaev & Pozanenko (2020b). Type I bursts are harder (higher value of $E_{\rm p,i}$) and fainter (lower value of $E_{\rm iso}$) than type II ones in general, therefore they are characterized by a higher value of EH parameter. For GRB 201015A, we obtain $EH = 0.49$, which is close to the most probable value of the type II bursts sample, $EH = 0.69$ (type I GRBs have $EH > 3.3$, in general).

The best possible separation of type I GRBs from type II ones is achieved in the coordinates of EH and $T_{90,\rm i}$ (duration in rest frame), which is shown in Fig. 4.The $T_{90,\rm i}$–EH diagram clearly classifies GRB 201015A as type II GRB, placed inside 68 per cent cluster region of type II bursts.

3.2 Afterglow

3.2.1 X-ray afterglow

The afterglow in the X-ray range was plotted on the basis of data that are publicly available on the *Swift* Burst Analyser website.[2] It consists of the data within ∼0.03–∼0.3 d time range and also includes a dot ∼20 d after the GRB 201015A trigger.

The available data do not allow to confirm the presence of any inhomogeneities since there are no X-ray observations of the light curve between the first and twentieth days. A joint power-law fit of all points gives a slope of 0.76 ± 0.03.

Late-time observations were carried out by *Chandra* X-ray Observatory 8.4 and 13.6 d after the trigger (Gompertz et al. 2020). The power-law decay between these two epochs was found to be ~ -0.8. This value is consistent with the *Swift*'s data approximation, which may also indicate the absence of any inhomogeneities in the X-ray light curve of the afterglow of the GRB 201015A.

[2] https://www.swift.ac.uk/burst_analyser/

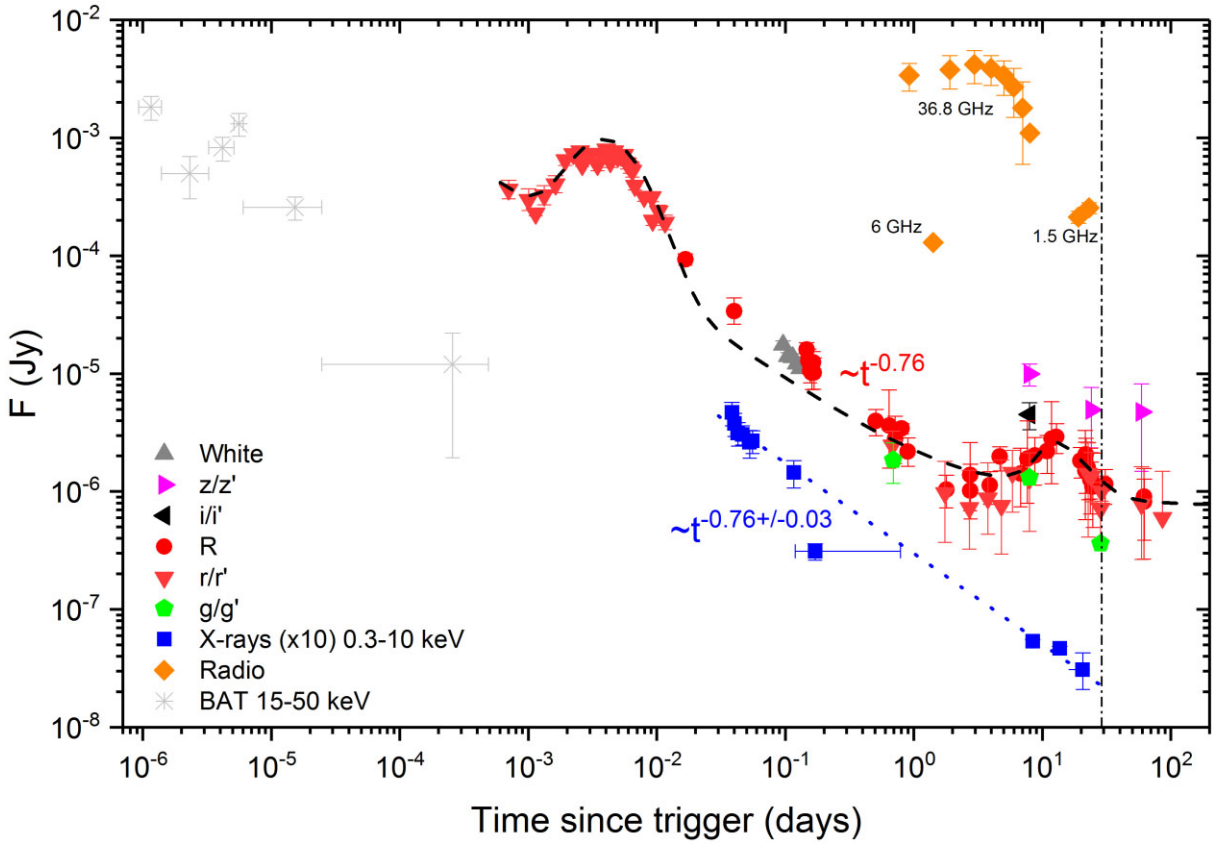

Figure 5. The complete multiwavelength light curve of GRB 201015A. All optical data are shown in Table B1. Radio observations at 36.8 GHz are shown in Table A1, while those at 1.5 and 6 GHz were taken from Rhodes et al. (2020) and Fong et al. (2020), respectively. The blue dotted line denotes an approximation of the *Swift*-XRT data. The black dashed line shows the joint approximation of the inhomogeneity at the stage of early afterglow, late afterglow, SN, and host galaxy (see Section 3.3.1). The data are not corrected for Galaxy extinction. The vertical dash–dotted line indicates the epoch when the spectrum was taken (see Section 3.3.2).

Chandra's observations were conducted in the 0.5–7 keV range. The unabsorbed flux values, recalculated for the energy range of 0.3–10 keV, which corresponds to *Swift*-XRT, are given by Giarratana et al. (2022). It can be seen that these points align well with the extrapolation of the *Swift*-XRT data spanning a time interval from 0.03 to 0.3 d. It confirms the absence of significant inhomogeneities in the X-ray afterglow. Therefore, this slope can be used to describe the optical afterglow.

Altogether X-ray data are shown in Fig. 5.

3.2.2 *Optical afterglow*

The data acquired during the optical observations were subjected to a standard preliminary reduction, including the rejection of defective frames, the reduction of frames using a bias matrix, a dark frame, a flat-field, and fringe removal, if necessary. The data reduction was performed with the IRAF[3] software package. The preliminary data reduction was carried out by the CCDPROC code of the package CCDRED; the individual images in the corresponding filters were then stacked by the IMCOMBINE code to provide the best signal-to-noise ratio (S/N). Aperture photometry was performed with the APPHOT code of the DAOPHOT package.

Obtaining a photometric solution for all epochs, from all instruments, and in all filters was achieved through mathematical flux subtraction. Given the close proximity of the source to several other objects simultaneously, direct isolation was barely possible. In this context, the method of template subtraction from scientific images did not allow for an accurate measurement of the source's magnitude due to observations being conducted with a wide array of different instruments. This variability arose from differences in pixel scales, which in most cases exceeded 0.7 arcsec pixel^{-1}, as well as variations in the limiting magnitudes depending on the instrument used. Consequently, image subtraction exhibited non-uniformity across all instruments. To mitigate this photometry inhomogeneity, the method of mathematical flux subtraction was employed. The following steps were covered. Aperture photometry was performed, with the radius of the aperture selected to encompass both the source, its host galaxy, and neighbouring blending objects, thereby capturing the total flux from all these sources. Throughout the observation period, only the flux of the GRB 201015A and SN 201015A associated with it displayed variations, while the luminosity of the host galaxy remained assumed to be constant. Measurements of magnitudes from nearby sources in GTC and Maidanak images showed no variability. Therefore, during the processing of each observation epoch, the contributions of neighbouring objects were subtracted, accounting

[3]IRAF (Image Reduction and Analysis Facility), an environment for image reduction and analysis, was developed and maintained by the National Optical Astronomy Observatory (Tucson, USA) operated by the Association of Universities for Research in Astronomy under cooperative agreement with the National Science Foundation of the USA, see iraf.noao.edu.

Table 3. Parameters of the early afterglow, afterglow, and SN components of optical light curve joint approximation after host subtraction and Galaxy extinction correction.

$A \times 10^{-5}$ (Jy)	ω_1	$x_c \times 10^{-3}$	$B \times 10^{-6}$ (Jy)	α	$C \times 10^{-6}$ (Jy)	t_0 (d)	τ_{fall} (d)	τ_{rise} (d)	D (Jy)	$\chi^2/d.o.f.$
1.14 ± 0.05	0.56 ± 0.03	5.4 ± 0.1	3.0 ± 0.3	0.77[a]	5.2 ± 3.8	10.2 ± 5.1	9.5 ± 7.7	1.6 ± 1.3	0[a]	1.9/72

[a]Parameter was fixed.

Table 4. The parameters of the SN 201015A estimated in this work.

M_V (mag)	T_{max} (d)	Type	v_{phot} (km s^{-1})	T_{bb} (K)
$-19.45^{+0.85}_{-0.47}$	8.54 ± 1.48	Ic	$1.1^{+2.0}_{-0.2} \times 10^4$	~5000

Table 5. GRB 201015A host galaxy information.

RA(J2000)	Dec.(J2000)	$m_{r'}$[a] (mag)	M_V (mag)
23:37:16.3110	+53:24:55.340	24.5	−17.40

[a]Not corrected for foreground or rest-frame extinction.

for the corresponding error transfer, and subsequently, the flux from the GRB 201015A and its host galaxy was determined. The results of this approach are depicted in the light curve presented in Fig. 5. The same approach was applied to the host galaxy's magnitude determination.

LBT/MODS imaging observations were taken in the Sloan filters g' and r' under good seeing conditions (0.″6) and were reduced using the data reduction pipeline developed at INAF – Osservatorio Astronomico di Roma (Fontana et al. 2014), which includes bias subtraction and flat-fielding, bad pixel and cosmic ray masking, astrometric calibration, and coaddition.

The measured instrumental magnitudes were calibrated against the SDSS–DR12 and USNO-B1.0 photometric catalogues. The reference stars were chosen according to the algorithm described in Skvortsov et al. (2016).

All optical observations are shown in Table B1 and encompass a time range of 60 s–85 d after the GRB trigger. It allows to construct the light curve shown in Fig. 5. It shows a significant inhomogeneity at the early afterglow stage in the form of a bump. Object brightness peaks about 5 min after the GRB trigger with $R \sim 16.5$ mag and then fades until the end of the current data set ~1 h after the trigger. Based on these observations, it was suggested that the inhomogeneity might be related more to the onset of the afterglow than to the reverse shock (see Ror et al. 2023).

After flare activity, the afterglow follows a single power-law decay. The slope was adopted from the X-ray range since no inhomogeneities are observed in it over a given time period. It was confirmed with several different instruments mentioned in Section 2.2. It is equal to −0.76 and this slope will be used during the joint approximation of early afterglow bump, afterglow, and SN components of the GRB 201015A's light curve.

Based on this approach, a second inhomogeneity becomes evident, occurring from 30 min to 7.2 h. It manifests itself as a positive deviation of the observation points from the afterglow approximation. However, due to data limitations, this cannot be either confirmed or refuted.

The values of the afterglow approximation parameters can be found in Table 3.

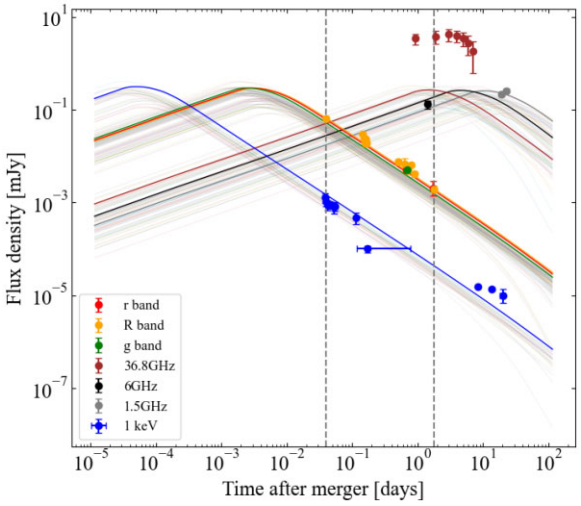

Figure 6. Multiwavelength afterglow light curves (see Section 3.2.3). For each band, the light curves predicted by the standard model are shown: r, R, and g bands (red, yellow, and green, respectively), 36.8 GHz (brown), 6 GHz (black), 1.5 GHz (grey), X-ray light curve (blue colour). The vertical lines pinpoint the epochs of the SEDs, illustrated in Fig. 7.

3.2.3 *Afterglow numerical modelling*

We attempt to model the multiwavelength afterglow of GRB 201015A using a Bayesian inference approach through a Markov Chain Monte Carlo (MCMC) code that explores the parameter space of synthetic afterglow realizations obtained with the publicly available PYTHON package AFTERGLOWPY (Ryan et al. 2020). AFTERGLOWPY is a PYTHON package for modelling GRB afterglows which computes synchrotron radiation from an external shock, allowing to take into account possible effects due to a jet structure and an off-axis observer position.

We model the full radio to X-ray data set of GRB 201015A by assuming a Gaussian model of the jet structure and fixing some of the parameters: an electron energy distribution power-law index of $p = 2.2$, the fraction of energy that goes into electrons and magnetic field of $\epsilon_e = 0.1$ and $\epsilon_B = 0.001$, respectively. We find best model of other parameters, with a 50 per cent (plus 84 per cent and minus 16 per cent) kinetic energy of $E_k = 2.0^{+3.8}_{-1.35} \times 10^{53}$ erg, a density of the surrounding interstellar medium of $n = 2 \times 10^{-3}$ cm^{-3}, a jet half-opening angle of the inner core of $\theta_j = 0.30^{+0.08}_{-0.12}$ rad, and a viewing angle of the observer with respect to the jet axis of $\theta_v = 0.31^{+0.30}_{-0.21}$ rad. The optical and X-ray data are well fitted by synchrotron radiation with a cooling frequency well above the X-ray range at the time the SN component is rising above the afterglow (Figure 6). This scenario is in line with the assumption of modelling the optical flux decay with the same rate measured in X-rays.

We note that this solution does not fit the light curve at 36.8 GHz which is an order of magnitude brighter than the modelled peak value. This might indicate the presence of an additional emission

component (e.g. a contribution from reverse shock) that we could not model in the framework of AFTERGLOWPY.

3.3 Supernova

The SN associated with GRB 201015A was detected in late photometric observations as an evident bump above the power-law afterglow decay (Pozanenko et al. 2020) and confirmed by spectroscopic observation (Rossi et al. 2021).

3.3.1 Light curve

Following the standard procedure, the detection of the SN can be accomplished by subtracting the contribution of the host galaxy and the afterglow from the observed optical light.

Since most of the observations were made in *r* and *R* filters, it was decided to reduce them to a single light curve. Using quasi-synchronous observations in the *R* filter at the Mondy, CrAO, and AbAO observatories and in the *r* filter at the ATO within the time span of ∼0.6–0.8 d after the GRB detection, the shift between these filters was determined. The points in the *R* filter were approximated, and the value was calculated at an epoch of 0.68081 d when we had observations in the *r* filter. By assuming that at this stage the source's luminosity decline is achromatic, we subtract the magnitude in the *R* filter from the magnitude in the *r* filter. From this procedure, the shift was determined. The photometric values taken with the *r* filter need to be brightened by 0.514 mag to match the *R* filter data.

The host galaxy's level was obtained based on late-time observations resulting in a determination of 24.5 mag in the r' filter. This contribution has been mathematically subtracted from the optical light curve.

The extinction in the Galaxy in the direction of the source is known ($A_R = 0.735$; based on Schlafly & Finkbeiner 2011) and has also been taken into account.

In order to distinguish the SN component, the estimation of the afterglow contribution should be done assuming that it is produced by synchrotron radiation in a relativistic shock interacting with a homogeneous external medium, as predicted by the classical fireball model (e.g. Sari, Piran & Narayan 1998; Zhang & Mészáros 2004).

Since no sufficient inhomogeneities are present in XRT afterglow during the first ∼8 d, its slope was utilized to approximate the late-time optical afterglow ($\sim t^{-0.76}$), while the early afterglow cannot be characterized by a single power law due to the presence of sufficient inhomogeneity (see Ror et al. 2023). Consequently, an approximation function was formulated to describe several parts of the optical light curve after host galaxy subtraction and Galaxy extinction correction simultaneously (equation 1):

$$F_\nu^{OT}(t) = F_\nu^{eAG}(t) + F_\nu^{AG}(t) + F_\nu^{SN}(t). \quad (1)$$

The individual components, namely the early afterglow bump, the afterglow itself, and the SN were approximated by the equations (2), (3), and (4), respectively:

$$F_\nu^{eAG}(t) = \frac{A}{\omega_1 x\sqrt{2\pi}} \exp -\frac{(\ln \frac{x}{x_C})^2}{2\omega_1^2}, \quad (2)$$

$$F_\nu^{AG}(t) = Bx^{-\alpha}, \quad (3)$$

$$F_\nu^{SN}(t) = C\frac{\exp -\frac{t-t_0}{\tau_{\rm fall}}}{1+\exp -\frac{t-t_0}{\tau_{\rm rise}}} + D. \quad (4)$$

The joint approximation of all stages of the light curve without Galaxy extinction correction and host galaxy subtraction is shown in Fig. 5. The values of the parameters after host subtraction and Galaxy extinction correction are presented in Table 3.

By employing the Bazin function (Bazin et al. 2011), which characterizes the SN component (equation 4), it becomes possible to determine the parameters defining the SN peak from the joint fit. This is the time from the onset of the burst to the maximum of the SN light curve in the observer's frame and the absolute magnitude at the maximum of the SN's brightness, corrected for Galaxy extinction.

Using the effective wavelength from Fukugita, Shimasaku & Ichikawa (1995), observer-frame *R* corresponds to rest-frame $634.9/(1+z) = 445.2$ nm. The effective wavelength of the *V* filter is 547.7 nm. The difference between $R_{\rm rest}$ and $V_{\rm obs}$ is 102 nm. To compare with other known SNe, we would need to use the *I* filter, because it would be closest to the *V* filter in the rest frame. However, since no observations were conducted in the *I* filter, we assume $R_{\rm obs} \approx V_{\rm rest}$ for SN/GRB's parameters comparison.

The obtained values of the time of maximum brightness after GRB trigger $T_{\rm max} = 8.45 \pm 1.48$ d (in a rest frame) and absolute magnitude $-19.45^{+0.85}_{-0.47}$ mag at maximum (Table 4) allow to compare it with other studied SN/GRBs cases. A comparison reveals that the SN 201015A exhibits the earliest peak among the described SN/GRB cases (e.g. Belkin et al. 2020a) and is in the middle of absolute magnitude distribution.

We can also estimate the absolute magnitude at the SN maximum using the results of numerical simulations of the afterglow with the AFTERGLOWPY described in Section 3.2.3. Using the afterglow contribution at ∼14.2 d after the trigger, we calculate it to be $-19.53^{+0.87}_{-0.20}$ mag. This is comparable to what was obtained by approximating the entire light curve with a multicomponent function and is also in consistency with what was presented by Patel et al. (2023).

A comparison of the SN 201015A with various broad-lined Ic SN associated with GRB is shown in Fig. 8. The comparison was carried out under the assumption that SNe were observed from the redshift $z = 1$ to compare them in the same frame. The decay rate of the SN 201015A most closely resembles that of SN 2016jca associated with GRB 161219B (Cano et al. 2017a). The closest overall light curve coincidence is seen for SN 2006aj associated with XRF 060 218 (Ferrero et al. 2006), particularly in the SN's dome, suggesting that their luminosity at the SN's maximum should be approximately equal.

3.3.2 Spectrum

We used both MODS-1 and MODS-2 in dual-grating mode (grisms G400L and G670L) providing a wavelength coverage from 3200–9500 Å and a slit mask with a width of 1 arcsec. The total integration time was 8 s × 900 s. The MODS data were reduced at the Italian LBT Spectroscopic Reduction Center[4] using scripts optimized for LBT data adopting the standard procedure for long-slit spectroscopy with bias subtraction, flat-fielding, bad-pixel correction, sky subtraction, and cosmic rays contamination. Wavelength calibration (in the air) was obtained using the spectra of Hg, Ar, Xe, and Kr lamps providing an accuracy of ∼0.08 Å over the whole spectral range. Relative flux calibration was derived from the observations of spectrophotometric standard stars.

All the spectra have been corrected for the Galactic extinction ($A_V = 0.93$). The low-S/N spectrum shows a peak around 540 nm (rest frame) and is consistent with Type Ic-BL SN spectra around

[4]http://www.iasf-milano.inaf.it/software

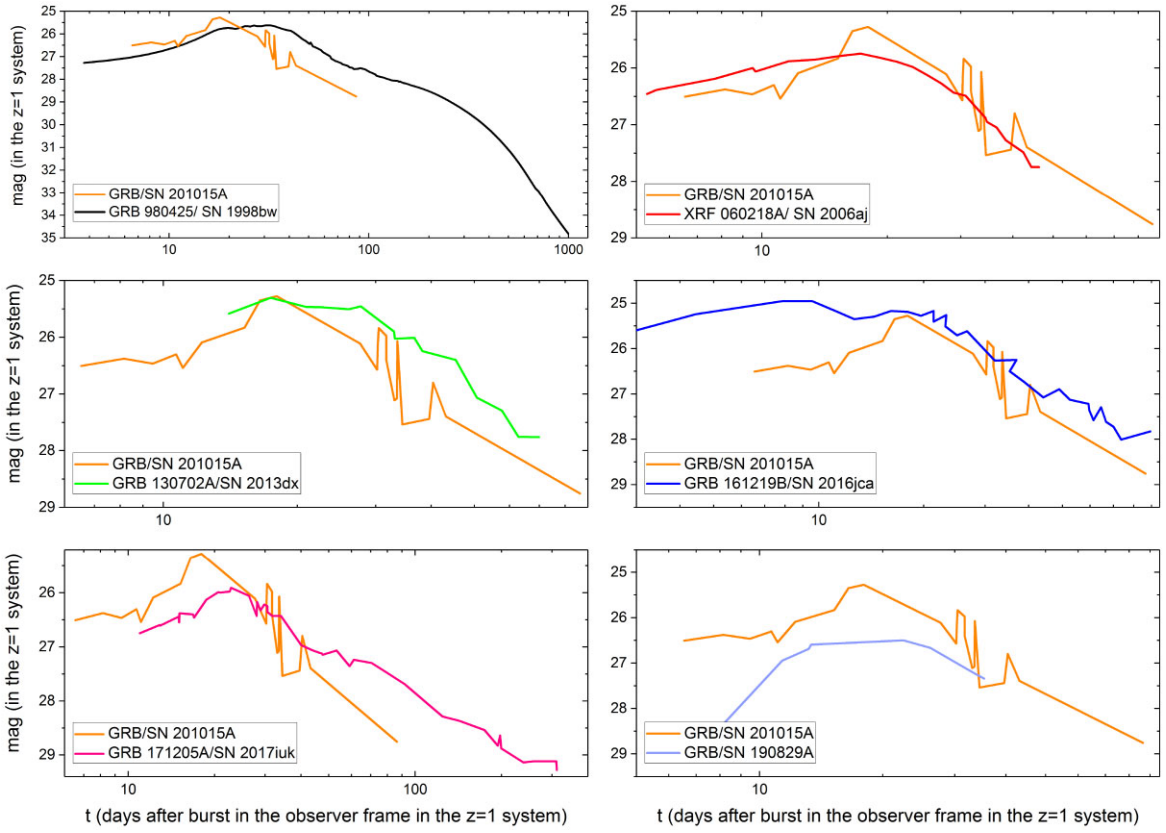

Figure 8. The light curve of the SN associated with the GRB 201015A compared to the known light curves of SN/GRB cases [GRB 980425/SN 1998bw: Clocchiatti et al. (2011); GRB 060218A/SN 2006aj: Ferrero et al. (2006); GRB 130702A/SN 2013dx: Volnova et al. (2017); GRB 161219B/SN 2016jca: Cano et al. (2017a); GRB 171205A/SN 2017iuk: Volnova et al. in prep.; GRB 190829A: Medler et al. in prep.]. Light curves are shown after recalculating them to $z = 1$. The afterglow and the host galaxy contribution were subtracted. All data were corrected for Galactic extinction (Schlafly & Finkbeiner 2011) and host galaxy extinction, where it was determined. As can be seen, the light curves of the SN 2016jca and the SN 2006aj have the most similarity with the light curve of the SN 201015A.

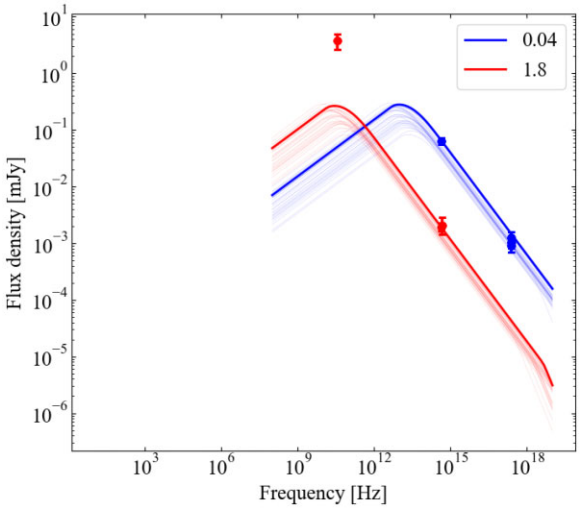

Figure 7. Spectral energy distribution of the GRB 201015A at epochs 0.04 and 1.8 d after detection. The results of the modelling are indicated by lines (see Section 3.2.3).

maximum light. The spectroscopic observations concur with the photometric discovery of the SN initially proposed in Pozanenko et al. (2020).

To obtain the photospheric velocity and identify the lines, modelling was carried out using the SYNOW code (e.g. Parrent, Branch & Jeffery 2010), which was previously employed to describe the spectra of both ordinary SNe and objects associated with GRBs. This code can be characterized by several assumptions, such as the spherically symmetric expansion of ejecta, the emission of light from a sharp photosphere (with lower velocity in the model), and the physical modelling of line profiles in which optical depths decrease exponentially with an e-folding velocity v_e ($\tau \propto e^{-v/v_e}$).

The slope of the central part of the spectrum (4000–6500 Å) was used to fit a blackbody continuum with the temperature $T_{bb} = 5000^{+3000}_{-1000}$ K. We excluded the edges of the spectrum, <4000 Å and >6500 Å, from the fitting process, as they can be affected by the presence of other lines (e.g. Ca II in the blue part) or instrumental problems.

It was possible to identify only the prominent lines of Fe II (S/N $\sim$ 2.4), which are usually observed in SN/GRB spectra. The slope within the range of 4800–5200 Å can be used for fitting the Fe II blend and estimating the photospheric velocity. The observed spectral detail can be described by the presence of Fe II expanding with velocities in the range from 5000 up to 30 000 km s^{-1}. However, the best model

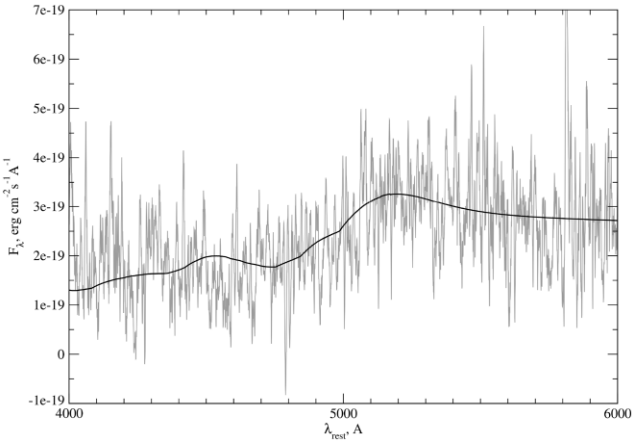

Figure 9. The resulting approximation of the SN 201015A spectrum using Fe II.

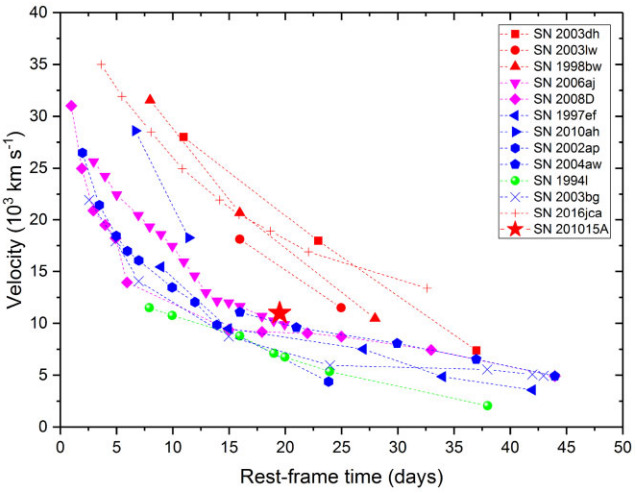

Figure 10. The photospheric velocity evolution with a rest-frame time given for 13 SNe. The red points are GRB–SN cases. The pink points are SNe associated with XRFs. The blue points are SNe unrelated to any of the mentioned high-energy events. SN 1994I is a normal SN Ic. References: Pian et al. (2006); Ashall et al. (2019); and Klose et al. (2019).

shows $v_{\rm ph} = 11\,000$ km s^{-1}, $v_{\rm e} = 20\,000$ km s^{-1}, and a temperature of 5000 K for this spectrum of SN 201015A.

Fig. 9 shows the observed spectrum and the model used to approximate it.

As a result of spectrum modelling, with a focus on the iron lines, the most satisfactory photospheric velocity was estimated to be 11 000 km s^{-1}. It might be compared with certain photospheric velocities for SNe of various types. Fig. 10 depicts the evolution of photospheric velocity over time for GRB-associated SNe, SNe with X-ray flashes (XRFs), and SNe with no relation to any of the transient events. Even taking into account large errors, it can be seen that the photospheric velocity for the SN 201015A still fits well with the fact that GRB–SNe have consistently higher photospheric velocities than standard events for the corresponding epoch.

3.4 Host galaxy

For the first time, the host of the GRB 201015A was identified in the several epochs of the stacked image during the SN's maximum stage (see Fig. 1). These observations were conducted with the 1.5-m telescope AZT-22 of the Maidanak Observatory on October 26, November 4 and 6. Total exposure was 61 s × 180 s. The pixel size (0.268 arcsec pixel^{-1}) and full width at half-maximum (∼0.8 arcsec) made it possible both to detect the source at coordinates consistent with those suggested by other research groups and to identify an object that is a candidate for the host galaxy. No sources within the coordinates of the proposed host (Table 5) were found in the catalogues (Sloan Digital Sky Survey, PanSTARRS, Legacy Survey). The most likely explanation is that the source's magnitude is fainter than the limiting magnitude of the images used to compile the catalogues.

The high quality of the stacked image enabled the determination of the source's offset relative to the host galaxy which is ∼1.5 arcsec. Assuming standard cosmology the scale would be 5.635 kpc arcsec^{-1}, equivalent to a projected distance of 8.453 kpc (Table 1).

In addition, late-time observations with the 1.5-m telescope AZT-20 of the ATO on 2021 January 9, were carried out. The total exposure was 160 s × 60 s. As a result of photometry and mathematical flux subtraction of the neighbouring objects (see Section 3.2.2), the host galaxy level was determined to be 24.5 mag in the r' filter.

Assuming that the surface distribution of galaxies adheres to a Poisson distribution, we can calculate the probability that a given galaxy is not associated with the GRB 201015A (e.g. Bloom, Kulkarni & Djorgovski 2002). With the given offset and the host's magnitude in the R filter after taking into account the Galaxy extinction, this probability is equal to 0.018. Consequently, it can be concluded that with a probability of 98.2 per cent this galaxy is the host galaxy for the GRB 201015A.

4 CONCLUSIONS

Its mostly quite challenging to spot an SN associated with a GRB, mainly because there are certain factors at play (e.g. distant source, bright host/afterglow; Belkin & Pozanenko 2023). At present, only about 50 SN/GRB cases were confirmed as a result of photometric observations, and there are an additional 27 GRBs where spectroscopic evidence has revealed SNe (with significant overlap between these two groups). Moreover, a detailed light curve, and even rarer, multicolour light curves, have only been constructed for a handful of such SNe. However, its crucial to emphasize that discovering an SN/GRB and studying its emissions can significantly enhance and advance our understanding of the GRB phenomenon. This underscores the importance of organizing quasi-continuous follow-up observations for each nearby (low redshift) GRB detected, with the primary goal of searching for its associated SN and potentially expanding our sample of such events.

As a result of an organized observational campaign of the GRB 201015A ($z = 0.426$) covering its prompt emission phase and over the course of approximately 85 d following the burst, the SN was discovered from a light curve of a source and subsequent spectroscopic observations allowed to confirm the presence of the SN and determine the time of maximum brightness after GRB trigger $T_{\rm max} = 8.45 \pm 1.48$ d (in a rest frame) and absolute magnitude $-19.45^{+0.85}_{-0.47}$ mag at maximum.

Through obtained photometric observations, crucial parameters of the SN 201015A were extracted. It is the absolute magnitude of the SN's light-curve maximum and the time of the peak from the GRB's detection in the rest frame. The comparison of these parameters with other known SN/GRB cases revealed that SN 201015A stands out as the earliest one, reaching peak luminosity in just ∼8.54 d after the

burst detection, while the median values of $T_{\rm max}$ across all SN/GRB's sample is about 14.2 d.

As a result of numerical modelling with the AFTERGLOWPY (Ryan et al. 2020), estimates of the main properties of the GRB jet and circumstellar medium were obtained ($E_k = 2.0^{+3.8}_{-1.35} \times 10^{53}$ erg, $n = 2 \times 10^{-3}$ cm^{-3}, $\theta_j = 0.30^{+0.08}_{-0.12}$, $\theta_v = 0.31^{+0.30}_{-0.21}$), as well as an estimate of the afterglow component to be subtracted from the SN emission was determined. Using it, the absolute magnitude of the SN's light-curve maximum was calculated and it coincides within the error with what was obtained by approximation of the light curve with a multicomponent function defined by equation (1).

A phenomenological comparison was conducted between the light curve of GRB 201015A and well-studied SN/GRBs light curves. In order to do this, all light curves were recalculated to the $z = 1$ system. Notably, the decay pattern of the SN 201015A bears a resemblance to that of SN 2016jca/GRB 161219B (Cano et al. 2017a). However, when considering the overall behaviour, SN 201015A's light curve closely mirrors that of SN 2006aj, which, in turn, is associated with the XRF 060218 (Ferrero et al. 2006).

Spectroscopic observations, on the other hand, enabled the identification of the flux excess on the ∼28.8 d as an SN Ic-BL (Rossi et al. 2021). Using the SYNOW code (e.g. Parrent, Branch & Jeffery 2010), the modelling of the obtained spectrum was carried out, determining the temperature of the blackbody component ($T_{\rm bb} \sim 5000$ K) and the photospheric velocity ($v_{\rm phot} \sim 11\,000$ km s^{-1}) on ∼16.5 d after the maximum of the light curve of the SN 201015A. The estimated value of the photospheric velocity does not contradict the distribution for this parameter determined for other SN/GRBs (Fig. 10). The value of photospheric velocity itself aligns most closely with the photospheric velocity of the SN 2006aj associated with the XRF 060218A for the respective epoch. Nevertheless, the large dispersion of values does not allow to draw reliable conclusions based on this.

The magnitude of the proposed host galaxy for GRB 201015A was determined through a mathematical flux subtraction procedure. Given the presence of multiple objects in close proximity to the host (see Fig. 1), straightforward photometry is quite a challenging process. Instead, we employed aperture photometry, encompassing all nearby objects within the aperture radius. Subsequently, we performed flux subtraction to isolate the host galaxy's contribution. This method gave a host galaxy flux value equivalent to 24.5 mag in the r' filter. We consider the galaxy as the host galaxy for GRB 201015A with a 98.2 per cent probability.

In addition to examining the optical counterpart, an analysis of the prompt emission phase (gamma-rays) of the GRB 201015A was conducted. Publicly available data from the *Fermi*-GBM experiment were used. The source remains undetectable above 50 keV due to its soft spectrum (e.g. Zhang et al. 2023). To classify the source, the method suggested in Minaev & Pozanenko (2020b) was applied, which relies on the $E_{\rm p,i}$–$E_{\rm iso}$ correlation. The source's position on the $E_{\rm p,i}$–$E_{\rm iso}$ and $T_{90,i}$–EH diagrams, as well as the value of the parameter $EH = 0.49$ classify GRB 201015A as a type II GRB.

ACKNOWLEDGEMENTS

SB, ASP, PYM, NSP, and AAV are grateful to the Russian Science Foundation (project no. 23-12-00220) for their partial support of the data reduction, analysis of data, and modelling. We also thank Sergei Blinnikov for useful discussion and suggestions regarding the article. AR acknowledges support from the INAF project Premiale Supporto Arizona & Italia. Spectroscopic data were obtained thanks to the programme IT-2019B-018 (P.I. A. Rossi). The LBT is an international collaboration among institutions in the United States, Italy, and Germany. LBT Corporation partners are The University of Arizona on behalf of the Arizona Board of Regents; Istituto Nazionale di Astrofisica, Italy; LBT Beteiligungsgesellschaft, Germany, representing the Max-Planck Society, The Leibniz Institute for Astrophysics Potsdam, and Heidelberg University; The Ohio State University, representing OSU, University of Notre Dame, University of Minnesota, and University of Virginia. GS acknowledges the support by the State of Hesse within the Research Cluster ELEMENTS (project ID 500/10.006). EVK is grateful to the Ministry of Science and Higher Education of Russian Federation for financial support (of the work); The AZT-33IK telescope is a part of Center for Common Use ≪Angara≫. VK and IVR were funded by the Aerospace Committee of the Ministry of Digital Development, Innovations and Aerospace Industry of the Republic of Kazakhstan (grant no. BR11265408). This work made use of data supplied by the UK Swift Science Data Centre at the University of Leicester.

DATA AVAILABILITY

The data presented in the paper would be sent on reasonable request to the corresponding author.

REFERENCES

Ackley K. et al., 2020, GCN Circ., 28639, 1
Amati L. et al., 2002, A&A, 390, 81
Ardeberg A., 1984. in Woltjer A., Ardeberg L. eds., Workshop on Site Testing for Future Large Telescopes. Garching bei München: European Southern Observatory, Garching bei München, p. 73
Ashall C. et al., 2019, MNRAS, 487, 5824
Barthelmy S. D. et al., 2005, Space Sci. Rev., 120, 143
Bazin G. et al., 2011, A&A, 534, A43
Belkin S., Pozanenko A., 2023, Pattern Recognit. Image Anal., 33, 86
Belkin S. O. et al., 2020a, Astron. Lett., 46, 783
Belkin S., Pankov N., Pozanenko A., Rumyantsev V., Volnova A., 2020b, GCN Circ., 28656, 1
Bennett C. L., Larson D., Weiland J. L., Hinshaw G., 2014, ApJ, 794, 135
Bloom J. S. et al., 1999, Nature, 401, 453
Bloom J. S., Kulkarni S. R., Djorgovski S. G., 2002, AJ, 123, 1111
Burrows D. N. et al., 2005, Space Sci. Rev., 120, 165
Cano Z. et al., 2017a, A&A, 605, A107
Cano Z., Wang S.-Q., Dai Z.-G., Wu X.-F., 2017b, Adv. Astron., 2017, 8929054
Chuprakov S. A., Eselevich M. V., Korobtsev I. V., 2018, J. Astron. Telesc. Instrum. Syst., 4, 024002
Clocchiatti A., Suntzeff N. B., Covarrubias R., Candia P., 2011, AJ, 141, 163
D'Ai A. et al., 2020, GCN Circ., 28660, 1
D'Elia V. et al., 2020, GCN Circ., 28632, 1
de Ugarte Postigo A., Kann D. A., Blazek M., Agui Fernandez J. F., Thoene C., Gomez Velarde G., 2020, GCN Circ., 28649, 1
Ehgamberdiev S. A., Baijumanov A. K., Ilyasov S. P., Sarazin M., Tillayev Y. A., Tokovinin A. A., Ziad A., 2000, A&AS, 145, 293
Elenin L., Kusakin A., Molotov I., 2015, Minor Planet Bull., 42, 27
Fan Z. et al., 2016, PASP, 128, 115005
Ferrero P. et al., 2006, A&A, 457, 857
Fletcher C., Veres P., Fermi-GBM Team, 2020, GCN Circ., 28663, 1
Fong W., Schroeder G., Rastinejad J., Hajela A., 2020, GCN Circ., 28688, 1
Fontana A. et al., 2014, A&A, 570, A11
Fukugita M., Shimasaku K., Ichikawa T., 1995, PASP, 107, 945
Galama T. J. et al., 1998, Nature, 395, 670
Garnavich P. M. et al., 2003, ApJ, 582, 924
Giarratana S. et al., 2022, A&A, 664, A36
Gompertz B. et al., 2020, GCN Circ., 28822, 1
Grossan B., Maksut Z., Kim A., Krugov M., Smoot G. F., Linder E., 2020, GCN Circ., 28674, 1

Hill J. M., Salinari P., 1994, in Stepp L. M., ed., Proc. SPIE Conf. Ser. Vol. 2199, Advanced Technology Optical Telescopes V. SPIE, Bellingham, p. 64
Hjorth J. et al., 2003, Nature, 423, 847
Hu Y. D. et al., 2020, GCN Circ., 28645, 1
Iwamoto K. et al., 1998, Nature, 395, 672
Izzo L., Malesani D. B., Zhu Z. P., Xu D., de Ugarte Postigo A., Pursimo T., 2020, GCN Circ., 28661, 1
Jelinek M. et al., 2020, GCN Circ., 28664, 1
Kennea J. A., Tagliaferri G., Campana S., Evans P. A., Osborne J. P., Burrows D., Swift-XRT Team, 2020, GCN Circ., 28635, 1
Khetsuriani T. S., 1967, Sol. Phys., 2, 237
Klose S. et al., 2019, A&A, 622, A138
Koshut T. M., Paciesas W. S., Kouveliotou C., van Paradijs J., Pendleton G. N., Fishman G. J., Meegan C. A., 1996, ApJ, 463, 570
Kouveliotou C., Meegan C. A., Fishman G. J., Bhat N. P., Briggs M. S., Koshut T. M., Paciesas W. S., Pendleton G. N., 1993, ApJ, 413, L101
Kulkarni S. R. et al., 1998, Nature, 395, 663
Kumar H. et al., 2020a, GCN Circ., 28680, 1
Kumar H., Stanzin U., Bhalerao V., Anupama G. C., Barway S., Growth-India Collaboration, 2020b, GCN Circ., 28681, 1
Lipunov V. et al., 2020, GCN Circ., 28633, 1
Malesani D. B., de Ugarte Postigo A., Pursimo T., 2020, GCN Circ., 28637, 1
Markwardt C. B. et al., 2020, GCN Circ., 28658, 1
Matheson T. et al., 2003, ApJ, 599, 394
Mazaeva E., Pozanenko A., Minaev P., 2018, Int. J. Mod. Phys. D, 27, 1844012
Minaev P. Y., Pozanenko A. S., 2020a, Astron. Lett., 46, 573
Minaev P. Y., Pozanenko A. S., 2020b, MNRAS, 492, 1919
Minaev P., Pozanenko A., 2020c, GCN Circ., 28668, 1
Minaev P. Y., Pozanenko A. S., 2021, MNRAS, 504, 926
Minaev P. Y., Pozanenko A. S., Loznikov V. M., 2010a, Astron. Lett., 36, 707
Minaev P. Y., Pozanenko A. S., Loznikov V. M., 2010b, Astrophys. Bull., 65, 326
Modjaz M., Liu Y. Q., Bianco F. B., Graur O., 2016, ApJ, 832, 108
Mozgunov G. Y., Minaev P. Y., Pozanenko A. S., 2021, Astron. Lett., 47, 150
Norris J. P., Bonnell J. T., 2006, ApJ, 643, 266
Paczyński B., 1998, ApJ, 494, L45
Parrent J., Branch D., Jeffery D., 2010, Astrophysics Source Code Library, record ascl:1010.055
Patel M. et al., 2023, MNRAS, 523, 4923
Pian E. et al., 2006, Nature, 442, 1011
Pogge R. W. et al., 2010, in McLean I. S., Ramsay S. K., Takami H., eds, Proc. SPIE Conf. Ser. Vol. 7735, Ground-Based and Airborne Instrumentation for Astronomy III. SPIE, Bellingham, p. 77350A
Pozanenko A. et al., 2020, GCN Circ., 29033, 1
Pozanenko A. S., Barkov M. V., Minaev P. Y., Volnova A. A., 2021, Astron. Lett., 47, 791
Prouza M., Jelínek M., Kubánek P., Ebr J., Trávníček P., Šmída R., 2010, Adv. Astron., 2010, 849382
Rastinejad J., Paterson K., Kilpatrick C. D., Fong W., 2020, GCN Circ., 28676, 1
Rhodes L., Fender R., Bray J., Williams D. R. A., 2020, GCN Circ., 28945, 1
Rodríguez-Espinosa J. M., Alvarez Martin P., 1997, in Ardeberg A. L., ed., Proc. SPIE Conf. Ser. Vol. 2871, Optical Telescopes of Today and Tomorrow. SPIE, Bellingham, p. 69
Roming P. W. A. et al., 2005, Space Sci. Rev., 120, 95
Ror A. K. et al., 2023, ApJ, 942, 32
Rossi A., Benetti S., Palazzi E., D'Avanzo P., D'Elia V., De Pasquale M., CIBO Collaboration, 2021, GCN Circ., 29306, 1
Rumyantsev V. V., Kiselev N. N., Ivanova A. V., 2019, Sol. Syst. Res., 53, 91
Ryan G., van Eerten H., Piro L., Troja E., 2020, ApJ, 896, 166
Sage L., 2003, in Heck A., ed., Astrophysics and Space Science Library, Vol. 296, Organizations and Strategies in Astronomy. Kluwer Academic Publishers, Dordrecht, p. 75
Sari R., Piran T., Narayan R., 1998, ApJ, 497, L17
Sari R., Piran T., Halpern J. P., 1999, ApJ, 519, L17
Schlafly E. F., Finkbeiner D. P., 2011, ApJ, 737, 103
Serebryanskiy A. V., Krugov M. A., Komarov A. A., Usol'tseva L. A., Akniyazov C. B., 2018, Sol. Syst. Res., 52, 320
Severny A. B., 1955, Vistas Astron., 1, 701
Shvedova G. S., 1995, Vistas Astron., 39, 273
Skvortsov N. A. et al., 2016, Astrophys. Bull., 71, 114
Stanek K. Z. et al., 2003, ApJ, 591, L17
Volnova A. A. et al., 2017, MNRAS, 467, 3500
Volvach A., Volvach L., Larionov M., 2023, Galaxies, 11, 96
Wright E. L., 2006, PASP, 118, 1711
Zhang B., Mészáros P., 2004, Int. J. Mod. Phys. A, 19, 2385
Zhang L.-L., Ren J., Wang Y., Liang E.-W., 2023, ApJ, 952, 127
Zhu Z. P., Liu X., Fu S. Y., Xu D., Gao X., Liu J. Z., 2020a, GCN Circ., 28653, 1
Zhu Z. P., Liu X., Fu S. Y., Xu D., 2020b, GCN Circ., 28677, 1

APPENDIX A: THE LOG OF THE RADIO OBSERVATIONS

Table A1. Log and results of the radio observations of the GRB 201015A.

UT Date	UT Time	t–T_0 (d)[a]	Frequency (GHz)	Flux (Jy)
2020-10-16	19:02–22:41	0.91770	36.8	0.0034 ± 0.0009
2020-10-17	19:14–21:54	1.90555	36.8	0.0038 ± 0.0012
2020-10-18	20:12–23:14	2.95347	36.8	0.0042 ± 0.0013
2020-10-19	21:08–23:54	3.98680	36.8	0.0039 ± 0.0011
2020-10-20	21:31–23:35	4.98819	36.8	0.0034 ± 0.0011
2020-10-21	21:03–23:03	5.96736	36.8	0.0027 ± 0.0012
2020-10-22	22:13–23:44	7.00590	36.8	0.0018 ± 0.0012
2020-10-23	21:21–23:14	7.97743	36.8	0.0011 ± 0.0013

[a]The mid-exposure time relative to the trigger time ($T_0 = 2459\,138.451\,539\,35$ JD).

APPENDIX B: THE LOG OF THE OPTICAL OBSERVATIONS

Table B1. GRB 201015A optical observation log. Magnitudes are in the AB (g', g, r, r', i', i, z', z) and Vega (R) systems, not corrected for foreground or rest-frame extinction.

UT Date	t–T_0 (d)[a]	Filter	Magnitude (mag)	Exposure (s)	Telescope	Source
15 Oct 2020	6.99E-04	r'	$17.49^{+0.20}_{-0.20}$	20	FRAM	Ror et al. (2023)
15 Oct 2020	9.99E-04	r'	$17.71^{+0.23}_{-0.23}$	20	FRAM	Ror et al. (2023)
15 Oct 2020	0.00113	r	$18.00^{+0.05}_{-0.05}$	3 × 40	NEXT	This work
15 Oct 2020	0.00132	r'	$17.61^{+0.21}_{-0.21}$	20	FRAM	Ror et al. (2023)
15 Oct 2020	0.00162	r'	$17.38^{+0.18}_{-0.18}$	20	FRAM	Ror et al. (2023)
15 Oct 2020	0.00193	r'	$16.87^{+0.11}_{-0.11}$	20	FRAM	Ror et al. (2023)
15 Oct 2020	0.00223	r'	$16.74^{+0.10}_{-0.10}$	20	FRAM	Ror et al. (2023)
15 Oct 2020	0.00252	r'	$16.68^{+0.10}_{-0.10}$	20	FRAM	Ror et al. (2023)
15 Oct 2020	0.00262	r	$16.97^{+0.03}_{-0.03}$	4 × 60	NEXT	This work
15 Oct 2020	0.00282	r'	$16.73^{+0.10}_{-0.10}$	20	FRAM	Ror et al. (2023)
15 Oct 2020	0.00312	r'	$16.73^{+0.10}_{-0.10}$	20	FRAM	Ror et al. (2023)
15 Oct 2020	0.00343	r'	$16.97^{+0.12}_{-0.12}$	20	FRAM	Ror et al. (2023)
15 Oct 2020	0.00373	r'	$16.75^{+0.10}_{-0.10}$	20	FRAM	Ror et al. (2023)
15 Oct 2020	0.00403	r'	$16.64^{+0.09}_{-0.09}$	20	FRAM	Ror et al. (2023)
15 Oct 2020	0.00433	r'	$16.90^{+0.12}_{-0.12}$	20	FRAM	Ror et al. (2023)
15 Oct 2020	0.00463	r'	$16.68^{+0.10}_{-0.10}$	20	FRAM	Ror et al. (2023)
15 Oct 2020	0.00493	r'	$16.79^{+0.11}_{-0.11}$	20	FRAM	Ror et al. (2023)
15 Oct 2020	0.00523	r'	$16.77^{+0.11}_{-0.11}$	20	FRAM	Ror et al. (2023)
15 Oct 2020	0.00553	r'	$16.75^{+0.10}_{-0.10}$	20	FRAM	Ror et al. (2023)
15 Oct 2020	0.00583	r'	$16.94^{+0.12}_{-0.12}$	20	FRAM	Ror et al. (2023)
15 Oct 2020	0.00613	r'	$17.01^{+0.13}_{-0.13}$	20	FRAM	Ror et al. (2023)
15 Oct 2020	0.00643	r'	$17.09^{+0.14}_{-0.14}$	20	FRAM	Ror et al. (2023)
15 Oct 2020	0.00673	r'	$17.41^{+0.09}_{-0.09}$	20	FRAM	Ror et al. (2023)
15 Oct 2020	0.00793	r'	$17.64^{+0.10}_{-0.10}$	20	FRAM	Ror et al. (2023)
15 Oct 2020	0.00913	r'	$17.65^{+0.09}_{-0.09}$	20	FRAM	Ror et al. (2023)
15 Oct 2020	0.00924	r	$18.15^{+0.10}_{-0.10}$	12 × 90	NEXT	This work
15 Oct 2020	0.01033	r'	$17.95^{+0.13}_{-0.13}$	20	FRAM	Ror et al. (2023)
15 Oct 2020	0.01154	r'	$18.19^{+0.16}_{-0.16}$	20	FRAM	Ror et al. (2023)
15 Oct 2020	0.01665	R	$18.79^{+0.12}_{-0.12}$	20	FRAM	Ror et al. (2023)
15 Oct 2020	0.03989	R	$19.88^{+0.28}_{-0.28}$	20	FRAM	Ror et al. (2023)
15 Oct 2020	0.09584	*White*	$20.27^{+0.08}_{-0.08}$	6 × 120	ZTSh	This work
15 Oct 2020	0.10470	*White*	$20.51^{+0.08}_{-0.08}$	6 × 120	ZTSh	This work
15 Oct 2020	0.11358	*White*	$20.54^{+0.07}_{-0.07}$	6 × 120	ZTSh	This work
15 Oct 2020	0.12243	*White*	$20.67^{+0.08}_{-0.08}$	6 × 120	ZTSh	This work
15 Oct 2020	0.13059	*White*	$20.77^{+0.08}_{-0.08}$	5 × 120	ZTSh	This work
15 Oct 2020	0.13799	*White*	$20.67^{+0.08}_{-0.08}$	5 × 120	ZTSh	This work
15 Oct 2020	0.14598	R	$20.70^{+0.15}_{-0.14}$	120	ZTSh	This work
15 Oct 2020	0.15143	R	$20.94^{+0.27}_{-0.25}$	120	ZTSh	This work
15 Oct 2020	0.15581	R	$21.15^{+0.26}_{-0.24}$	120	ZTSh	This work
15 Oct 2020	0.16017	R	$21.19^{+0.36}_{-0.33}$	120	ZTSh	This work
15 Oct 2020	0.16382	R	$20.97^{+0.24}_{-0.22}$	120	ZTSh	This work
15 Oct 2020	0.16675	R	$21.19^{+0.35}_{-0.32}$	120	ZTSh	This work
16 Oct 2020	0.50417	R	$22.21^{+0.31}_{-0.24}$	9 × 300	2.16-m	This work
16 Oct 2020	0.64075	R	$22.31^{+0.91}_{-0.75}$	30 × 120	AZT-33IK	This work
16 Oct 2020	0.68081	r'	$22.91^{+0.39}_{-0.30}$	38 × 60	AZT-20	This work

Table B1 – *continued*

UT Date	t–T_0 (d)[a]	Filter	Magnitude (mag)	Exposure (s)	Telescope	Source
16 Oct 2020	0.68796	g'	$23.23^{+0.37}_{-0.49}$	36 × 60	AZT-20	This work
16 Oct 2020	0.69640	i'	$21.93^{+0.32}_{-0.43}$	38 × 60	AZT-20	This work
16 Oct 2020	0.71278	R	$22.59^{+0.52}_{-0.48}$	108 × 30	AC-32	This work
16 Oct 2020	0.80396	R	$22.38^{+0.11}_{-0.11}$	87 × 120	ZTSh	This work
16 Oct 2020	0.89426	Rc	$22.86^{+0.32}_{-0.29}$	12 × 300	Zeiss-1000 (S)	This work
17 Oct 2020	1.73782	r'	$23.92^{+1.05}_{-0.66}$	75 × 60	AZT-20	This work
17 Oct 2020	1.78383	Rc	$23.67^{+0.39}_{-0.31}$	12 × 300	Zeiss-1000 (S)	This work
18 Oct 2020	2.70303	r'	$24.24^{+0.88}_{-0.80}$	53 × 60	AZT-20	This work
18 Oct 2020	2.73227	R	$23.36^{+0.76}_{-0.69}$	34 × 120	AZT-33IK	This work
18 Oct 2020	2.74040	R	$23.69^{+0.60}_{-0.56}$	198 × 30	AC-32	This work
19 Oct 2020	3.74775	r'	$24.04^{+0.76}_{-0.76}$	97 × 60	AZT-20	This work
19 Oct 2020	3.89597	R	$23.58^{+0.41}_{-0.29}$	8 × 300	AZT-22	This work
20 Oct 2020	4.66042	R	$22.97^{+0.31}_{-0.20}$	12 × 300	AZT-22	This work
20 Oct 2020	4.78555	r'	$24.20^{+1.02}_{-0.97}$	77 × 60	AZT-20	This work
21 Oct 2020	5.81591	r'	$23.50^{+0.84}_{-0.48}$	71 × 60	AZT-20	This work
22 Oct 2020	6.75409	R	$23.33^{+0.71}_{-0.54}$	68 × 60	AZT-33IK	This work
23 Oct 2020	7.61789	R	$23.02^{+0.95}_{-0.80}$	69 × 60	AZT-33IK	This work
23 Oct 2020	7.88468	g	>23.6	180	GTC	This work
23 Oct 2020	7.88765	r	$23.62^{+1.12}_{-0.55}$	180	GTC	This work
23 Oct 2020	7.89064	i	$22.26^{+0.32}_{-0.26}$	180	GTC	This work
23 Oct 2020	7.89430	z	$21.40^{+0.26}_{-0.21}$	300	GTC	This work
24 Oct 2020	8.70510	R	$22.95^{+0.62}_{-0.39}$	21 × 60	Zeiss-1000 (T)	This work
26 Oct 2020	10.84952	R	$22.86^{+0.47}_{-0.34}$	19 × 180	AZT-22	This work
28 Oct 2020	11.75488	R	$22.59^{+0.96}_{-0.78}$	90 × 60	AZT-33IK	This work
28 Oct 2020	12.81643	R	$22.55^{+0.36}_{-0.28}$	27 × 180	AZT-22	This work
04 Nov 2020	19.73793	R	$23.06^{+0.37}_{-0.28}$	27 × 180	AZT-22	This work
06 Nov 2020	21.55624	R	$23.27^{+1.03}_{-0.86}$	48 × 60	AZT-33IK	This work
06 Nov 2020	21.62762	R	$23.08^{+0.67}_{-0.42}$	30 × 150	Zeiss-1000 (T)	This work
06 Nov 2020	21.72694	R	$22.93^{+0.49}_{-0.35}$	15 × 240	AZT-22	This work
07 Nov 2020	22.61255	R	$23.21^{+0.67}_{-0.54}$	30 × 120	AZT-33IK	This work
07 Nov 2020	22.61255	r'	$23.52^{+1.34}_{-0.66}$	56 × 60	AZT-20	This work
08 Nov 2020	23.57483	R	$23.46^{+0.73}_{-0.67}$	30 × 120	AZT-33IK	This work
08 Nov 2020	23.87368	Rc	$23.45^{+0.42}_{-0.36}$	11 × 300	Zeiss-1000 (S)	This work
08 Nov 2020	23.94498	r	$23.57^{+0.54}_{-0.51}$	540	GTC	This work
08 Nov 2020	23.95339	z	$22.16^{+0.81}_{-0.47}$	600	GTC	This work
09 Nov 2020	24.56936	R	$23.61^{+0.87}_{-0.71}$	30 × 120	AZT-33IK	This work
13 Nov 2020	28.22051	r	$24.26^{+0.81}_{-0.69}$	14 × 120	LBT	This work
13 Nov 2020	28.22054	g	>25	14 × 120	LBT	This work
13 Nov 2020	28.80000	r	$23.89^{+0.20}_{-0.20}$	14 × 120	LBT	This work
15 Nov 2020	30.77597	R	$23.56^{+0.42}_{-0.31}$	15 × 240	AZT-22	This work
13 Dec 2020	58.87929	r	$24.17^{+1.17}_{-0.79}$	540	GTC	This work
13 Dec 2020	58.88762	z	$22.21^{+1.26}_{-0.60}$	600	GTC	This work
16 Dec 2020	61.64333	R	$23.82^{+1.32}_{-0.60}$	69 × 120	AZT-33IK	This work
16 Dec 2020	61.67941	R	$23.93^{+0.81}_{-0.48}$	6 × 240	AZT-22	This work
09 Jan 2021	85.67848	r'	$24.45^{+n/d}_{-0.99}$	160 × 60	AZT-20	This work

[a]The mid-exposure time relative to the trigger time ($T_0 = 2459\,138.451\,539\,35$ JD).

[1]*National Research University 'Higher School of Economics', Faculty of Physics, Myasnitskaya ul. 20, Moscow 101000, Russia*
[2]*Space Research Institute of the Russian Academy of Sciences, Profsoyuznaya ul. 84/32, Moscow 117997, Russia*
[3]*School of Physics and Astronomy, Monash University, Clayton, VIC 3800, Australia*
[4]*Institute of Physics and Technology, Institutskiy Pereulok, 9, Dolgoprudny 141701, Russia*
[5]*P.N. Lebedev Physical Institute of the Russian Academy of Sciences, 53 Leninsky Avenue, 119991 Moscow, Russia*
[6]*INAF – Osservatorio di Astrofisica e Scienza dello Spazio, via Piero Gobetti 93/3, I-40129 Bologna, Italy*
[7]*Institut für Theoretische Physik, Goethe Universität, Max-von-Laue-Str 1, D-60438 Frankfurt am Main, Germany*
[8]*Istituto di Astrofisica e Planetologia Spaziali, via Fosso del Cavaliere 100, I-00133 Roma, Italy*
[9]*INAF – Osservatorio Astronomico di Padova, Vicolo dell'Osservatorio 5, I-35122 Padova, Italy*
[10]*Special Astrophysical Observatory of the Russian Academy of Sciences (SAO RAS), Nizhnij Arkhyz 369167, Russia*
[11]*Ulugh Beg Astronomical Institute (UBAI) of the Uzbek Academy of Sciences, 33 Astronomicheskaya str, Tashkent 100052, Uzbekistan*
[12]*Crimean Astrophysical Observatory, Russian Academy of Sciences, Nauchnyi 298409, Russia*
[13]*Institute of Solar-Terrestrial Physics, Russian Academy of Sciences, Siberian Branch, Irkutsk 664033, Russia*
[14]*Evgeni Kharadze Georgian National Astrophysical Observatory, Adigeni, Abastumani 0301, Georgia*
[15]*Fesenkov Astrophysical Institute, Observatory street 23, Almaty 050020, Kazakhstan*
[16]*Pulkovo Observatory, Russian Academy of Sciences, Saint Petersburg 196140, Russia*
[17]*Instituto de Astrofísica de Andalucúa (IAA-CSIC), Apartado de Correos, 3.004, E-18.080 Granada, Spain*
[18]*Instituto de Astrofísica de Andalucía (IAA-CSIC), Glorieta de la Astronomía s/n, E-18008 Granada, Spain*
[19]*CAS Key Laboratory of Space Astronomy and Technology, National Astronomical Observatories, Chinese Academy of Sciences, Beijing 100101, China*

This paper has been typeset from a TEX/LATEX file prepared by the author.